Monthly Notices of the ROYAL ASTRONOMICAL SOCIETY

MNRAS **452,** 3304–3318 (2015) doi:10.1093/mnras/stv1558

The structure and dynamics of the AC114 galaxy cluster revisited

Dominique Proust,[1⋆] Irina Yegorova,[2] Ivo Saviane,[2] Valentin D. Ivanov,[2] Fabio Bresolin,[3] John J. Salzer[4] and Hugo V. Capelato[5,6]

[1]*Observatoire de Paris-Meudon, GEPI, F-92195 MEUDON, France*
[2]*European Southern Observatory, Alonso de Cordova 3107, Vitacura, Casilla 19001, Santiago de Chile 19, Chile*
[3]*Institute for Astronomy, 2680 Woodlawn Drive Honolulu, HI 96822, USA*
[4]*Department of Astronomy, Indiana University, 727 East Third Street, Bloomington, IN 47405, USA*
[5]*Divisão de Astrofísica, INPE-MCT, 12227-010 São José dos Campos, São Paulo, SP, Brazil*
[6]*Núcleo de Astrofísica Teóretica, Universidade Cruzeiro do Sul, rua Galvão Bueno 868, CEP 01506-200, São Paulo, SP, Brazil*

Accepted 2015 July 10. Received 2015 July 9; in original form 2014 May 16

ABSTRACT

We present a dynamical analysis of the galaxy cluster AC114 based on a catalogue of 524 velocities. Of these, 169 (32 per cent) are newly obtained at European Southern Observatory (Chile) with the Very Large Telescope and the VIsible MultiObject spectrograph. Data on individual galaxies are presented and the accuracy of the measured velocities is discussed. Dynamical properties of the cluster are derived. We obtain an improved mean redshift value $z = 0.31665 \pm 0.0008$ and velocity dispersion $\sigma = 1893^{+73}_{-82}$ km s^{-1}. A large velocity dispersion within the core radius and the shape of the infall pattern suggests that this part of the cluster is in a radial phase of relaxation with a very elongated radial filament spanning 12 000 km s^{-1}. A radial foreground structure is detected within the central 0.5 h^{-1} Mpc radius, recognizable as a redshift group at the same central redshift value. We analyse the colour distribution for this archetype Butcher–Oemler galaxy cluster and identify the separate red and blue galaxy sequences. The latter subset contains 44 per cent of confirmed members of the cluster, reaching magnitudes as faint as R_f= 21.1 (1.0 mag fainter than previous studies). We derive a mass $M_{200} = (4.3 \pm 0.7) \times 10^{15}$ M$_\odot$ h^{-1}. In a subsequent paper, we will utilize the spectral data presented here to explore the mass–metallicity relation for this intermediate redshift cluster.

Key words: galaxies: clusters: general – galaxies: distances and redshifts – galaxies: evolution – cosmology: observations – distance scale – large-scale structure of Universe.

1 INTRODUCTION

Redshift surveys of clusters of galaxies are needed to study their dynamical and evolutionary state. In clusters, the mean redshift is a key ingredient in deriving distances, allowing the study of matter distribution on very large scales. Analysis of the velocity distribution within clusters can lead to an estimate of the virial mass, constraining models of the dark matter content. Dynamical mass estimates complement measurements at other wavelengths, in particular those obtained through X-ray observations of clusters. However, discrepancies between optical, spectroscopic and X-ray mass estimators are often found (e.g. Girardi et al. 1998; Allen 2000; Cypriano et al. 2005). Virial mass estimates rely on the assumption of dynamical equilibrium. X-ray mass estimates also depend on the dynamical equilibrium hypothesis and on the still not well-constrained intracluster gas temperature gradient (e.g. Leccardi & Molendi 2008) although it is much better established from both *Chandra* and *XMM* data analyses. Finally, mass estimates based on gravitational lensing are considered more reliable than the others (e.g. Mellier 1999) because they are completely independent of the dynamical status of the cluster. The drawback is that lensing cannot probe the mass profile beyond the virial radius of clusters. The discrepancies among the methods may come from the non-equilibrium effects in the central region of the clusters (Allen 1998).

In this paper, we build upon previous studies of the dynamical status of the cluster AC114 with the addition of a new set of velocities. The observations of radial velocities reported here are part of a program to study the mass–metallicity relation (MZR) in AC114 (Saviane et al. 2014; Saviane et al., in preparation), which is a powerful diagnostic of galaxy evolution, as first shown by Larson (1974). Note that the sensitivity of available instruments at 10m-class telescopes does not allow for the accurate determination of the MZR at the highest redshifts, but for AC114 at $z \sim 0.32$ we are able to measure abundances reliably.

The AC114 cluster (RA = $22^h58^m52^s.3$ Dec. = $-34°46'55''$ J2000) is classified as Bautz–Morgan type II–III by Abell, Corwin & Olowin (1989). It is the archetype object of the Butcher–Oemler

⋆E-mail: dominique.proust@obspm.fr

(BO) effect with a higher fraction of blue, late-type galaxies than in lower redshift clusters, rising to 60 per cent outside the core region (Couch et al. 1998; Sereno, Lubini & Jetzer 2010).

AC114 has 724 galaxies listed in SIMBAD in an area of ∼10 arcmin × 10 arcmin, and 585 of them are classified as emission-line galaxies. It has been observed several times. For example, Couch & Sharples (1987) derived 51 velocities (42 cluster members), Couch et al. (2001) with 51 Hα emitting cluster members, and more recently in the 2dF survey (Colless et al. 2003) and the 6dF survey (Jones et al. 2009). A total of 308 velocities are available in the NASA/IPAC Extragalactic Database (NED) within a 10 arcmin radius, 348 within 20 arcmin and 414 within 30 arcmin. AC114 has a compact core dominated by a cD galaxy and a strong lensing power with several bright arcs and multiple image sources (Smail et al. 1995; Natarajan et al. 1998; Campusano et al. 2001). It is a hot X-ray emitter ($kT = 8.0$ keV) with an irregular morphology. Below 0.5 keV, the X-ray emission is dominated by two main components: the cluster, roughly centred on the optical position of AC 114, and a diffuse tail, extending almost 400 kpc from the cluster centre to the south-east. The cD galaxy is shifted with respect to the centroid of the X-ray emission but aligned in the general direction of the X-ray brightness elongation (see de Filippis et al. 2004). An extensive study of AC114 based on a multiwavelength strong lensing analysis of baryons and dark matter from Sereno et al. (2010) provided evidence of dynamical activity, with the dark matter distribution being shifted and rotated with respect to the gas, following the galaxy density in terms of both shape and orientation. Based on the lensing and X-ray data, they argue that the cluster extends in the plane of the sky and is not affected by the lensing overconcentration bias. As our observations increase by 32 per cent the data available for this cluster, we expand the dynamical analysis of AC114 in this paper. The MZR is developed in Saviane et al. (2014) and Saviane et al. (in preparation).

We present in Section 2 the details of the observations and data reduction. In Section 3, we discuss the distribution and the velocity analysis of the cluster galaxies. Section 4 describes the kinematical structures of AC114 and Section 5 makes the analysis of the distribution in colour and the BO effect while in Section 6 we analyse the dynamical mass determinations of AC114. We summarize our conclusions in Section 7. We adopt here, whenever necessary, $H_0 = 100\,h$ km s^{-1} Mpc^{-1}, $\Omega_{\rm M} = 0.3$ and $\Omega_\Lambda = 0.7$.

2 OBSERVATIONS AND DATA REDUCTIONS

The observations were carried out in service mode with the VIsible MultiObject Spectrograph (VIMOS; Le Fèvre et al. 2003) mounted on the Very Large Telescope (VLT), ESO (083.A-0566). VIMOS is a visible light (360–1000 nm) wide field imager and multiobject spectrograph mounted on the Nasmyth focus B of UT3 Melipal. The instrument is made of four identical arms each with a field of view of 7 arcmin × 8 arcmin, and a 0.205 arcsec pixel size. There is an ∼2 arcmin gap between the quadrants. Each arm is equipped with six grisms providing a spectral resolution range from ∼200 to 2500 and with one EEV 4k × 2k CCD. Two dispersion modes were used: MR grating (spectral resolution of 580 for a 1 arcsec slit, over 500–1000 nm spectral range) and HR-red grating (spectral resolution of 2500 for a 1 arcsec slit, over 630–870 nm spectral range). The galaxy selection was made from the pre-imaging frames of the cluster. To construct the masks, initially, the SIMBAD catalogue was used without imposing any restriction criterion. As a first step we identified already known galaxies of the cluster. Then we selected the non-stellar objects in this region by eye in order to punch a maximum number of slits in each of the four quadrants. Such a visual inspection allows us to discriminate between extended objects and stars.

Table 1. Observing blocks of AC114.

OB_{ID}	Date	OB start[a]	Exp. time[b]	Filter	Grism
382919	2009-09-17	02:37	2250	GG475	HR red
382920	2009-09-17	03:32	2250	GG475	HR red
382921	2009-09-17	04:11	2250	GG475	HR red
382922	2009-09-17	04:50	2250	GG475	HR red
382923	2009-09-17	05:28	2250	GG475	HR red
382924	2009-09-17	06:07	2250	GG475	HR red
382925	2009-09-21	03:54	2250	GG475	HR red
382926	2009-08-16	05:25	2250	GG475	MR
382927	2009-08-16	06:15	2250	GG475	MR
382928	2009-08-16	06:55	2250	GG475	MR
382929	2009-08-21	07:24	2250	GG475	MR
382930	2009-08-21	06:11	2250	GG475	MR
382931	2009-09-25	04:02	2250	GG475	MR
382932	2009-09-25	04:53	2250	GG475	MR

Notes. [a]beginning of the observation block, UT time.
[b]exposure time of the science part, in seconds.

The 14 awarded hours of observations were done on 2009 August 16 and 21, and September 17, 21 and 25 (see Table 1). Execution time for each observing block was 60 min, including 22.5 min of overheads. Observing blocks were prepared for both MR and HR-red grisms. For each grism observing block was repeated seven times. The total integration time on target galaxies is 4.37 h for each grism.

Fig. 1 shows the projected map in RA and Dec. of our program galaxies in AC114 out to a velocity $cz = 120\,000$ km s^{-1}. Note that most of the objects in the central part represent four clumps corresponding to the four VIMOS quadrants of a VLT mask. The other galaxies spread in the field are objects already observed with velocities published in the literature.

The data reduction was carried out independently at European Southern Observatory (ESO)-Santiago and Paris-Meudon

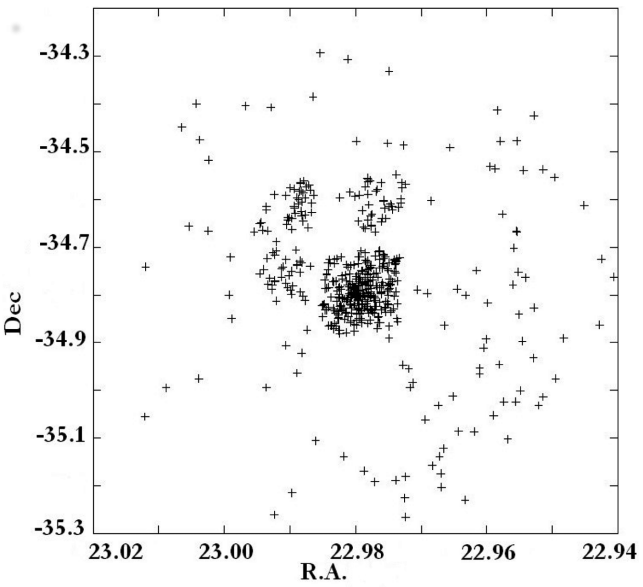

Figure 1. Map of the AC114 galaxies with observed velocities. The four central clumps are VIMOS observations at the VLT while galaxies spread in the field are from the literature.

observatory in order to obtain wavelength and flux calibrated spectra. Thanks to the double reduction of the data, we could compare the quality of the results. At ESO-Santiago we used the VIMOS pipeline to reduce the data. We reduced separately the data taken with the grism HR red and MR. Each scientific frame was bias subtracted and flat-field corrected, the cosmic rays were removed, and sky emission lines subtracted (the same procedure was done for the standard stars). The spectra were wavelength calibrated and seven frames for each VIMOS quadrant were combined. This gave us S/N = 20 per pixel on the average at the continuum level on the final spectra. Since the continuum of most of the galaxies is too weak we did not use the spectra extracted by the pipeline. Instead, we extracted one-dimensional spectra with MIDAS.

At Meudon, we independently reduced the data with the MULTIRED package (Le Fèvre et al. 1995) of IRAF[1] performing the following steps in sequence for each slit.

– Extract small 2D postage-stamp images corresponding to one slit from the two-dimensional spectra of the object and the corresponding wavelength calibration and flat-field from the full 4k × 2k pixel images.

– For each two-dimensional spectrum correct for flat-field (pixel to pixel variation) and subtract sky emission: the sky is fitted with adjustable low-order polynomials, and subtracted along the slit for each wavelength element. A treatment of the zero-order position was also added: areas on the two-dimensional spectra with a zero order could be corrected independently from the rest of the spectrum, if needed.

– Combine all the corrected two-dimensional spectra of a given object with average or median scheme using sigma-clipping rejection. This removes most of the cosmic ray events, although in some circumstances, the brightest events can still partially remain.

– Extract a one-dimensional spectrum of the arc-lamps and cross-correlate with a reference arc-lamp spectrum to produce an initial wavelength solution. The fit was then adjusted, if necessary. This produces a unique pixel/wavelength transformation for each slit.

– Extract a one-dimensional spectrum from the corrected two-dimensional spectrum for each object of interest in the slit by averaging along the wavelength axis.

– Wavelength and flux calibrate the one-dimensional object spectrum. We observed the F-type standard star LTT1788 ($V = 13.16$, $B - V = +0.47$) and the DA-type LTT7987 ($V = 12.23$, $B - V = +0.05$) from Hamuy et al. (1992, 1994).

– Plot the corrected and calibrated one-dimensional spectrum and display all the corrected two-dimensional spectra together with the averaged two-dimensional spectrum. Line identification for redshift measurement can then proceed.

Because of the lack of CCD photometry for this cluster, we collected UK-J B_j and ESO-R or POSS-I E R_f magnitudes from superCOSMOS (Maddox, Efstathiou & Sutherland 1990a; Maddox et al. 1990b); The photometric accuracy of these data is typically 0.3 mag with respect to external data for $m \succ 15$. Colours ($B - R$ or $R - I$) are externally accurate to 0.07 mag at $B_j = 16.5$ rising to 0.16 mag at $B_j = 20$. B_j and R_f magnitudes are listed in Table 2. Looking at this table, the faintest objects for which superCOSMOS provides an apparent magnitude estimate have magnitudes $B_j = 22.6$ and $R_f = 21.1$. However, it is also clear that luminosities are not available for roughly fifty per cent of our targets. To overcome this limitation, we obtained a relation between the integrated flux of our spectra and the R_f magnitude, and then the relation was applied to get a first estimate of the R_f magnitude for objects that do not have a luminosity estimate.

The flux integral was computed simply as $\Sigma f \times \delta\lambda$, where f is the flux in units of 10^{-16} erg cm^{-2} s^{-1} Å^{-1} and $\delta\lambda = 2.6$ Å is the spectral bin. The flux integral was limited to the common spectral range of the spectra, which is from 4897.5 to 9785.5 Å. The relation between the integrated flux and R_f is shown in Fig. 2. Assuming that the relation is linear, with a preliminary fit we found that the slope of the regression is ∼2.7, which suggests that our integrated flux is close to what is measured by the R-band photometry. Therefore, we imposed the relation to be $R_f = -2.5 \log f + R_0$ and we found $R_0 = 25.62$, with a dispersion of 0.51 dex around the fit.

The dispersion is quite satisfactory for an order-of-magnitude estimate of galaxian luminosities, and it is likely due to object-to-object variations in slit losses, night-to-night differences in the flux calibration of the VIMOS spectra, and variable sky transparency in the course of the observations.

Using the relation above, for each galaxy an $R_{\rm comp}$ magnitude can be computed, and luminosity distributions can be produced. In Fig. 3, we show such distributions for 25 galaxies that already have a spectrum in the literature as flagged by an entry in the NED,[2] and for 138 galaxies added with this work. No selection was done; this work covers a larger area than older data sets. The apparent magnitude distribution of galaxies with existing spectra turns over at $R_{\rm comp} \sim 19$ while that of our new sample keeps growing down to $R_{\rm comp} \sim 20$. Below $R_{\rm comp} \sim 19$ the literature sample thus suffers from incompleteness compared to our new sample, which reaches ∼1 mag deeper than existing data. The mismatch between the R_f and $R_{\rm comp}$ sensitivity/integration bands may also contribute to the dispersion in the relation.

In order to study the completeness of our catalogue, we compared it to the corresponding superCOSMOS plate[3] (Hambly, Irwin & MacGillivray 2001) as our faintest program galaxies are close to the superCOSMOS limiting magnitude ($\simeq B_j = 23.0$ and $R_f = 21.5$). In the core radius $R_c = 1.02$ arcmin (0.27 h^{-1} Mpc see Couch & Sharples 1987), all of the eight galaxies have velocities. In the Abell radius computed above $R_{\rm Abell} = 5.431$ arcmin (1.44 h^{-1} Mpc), 109 out of 173 galaxies (63 per cent) have velocities and in the virial radius $R_v = 3.0$ h^{-1} Mpc (see Couch et al. 2001) 340 out of 724 galaxies (47 per cent) have velocities.

Radial velocities have been determined using the cross-correlation technique (Tonry & Davis 1979) implemented in XCSAO task of the RVSAO package (Kurtz et al. 1991; Mink & Wyatt 1995) with spectra of radial velocity standards of late-type stars (Pickles 1998) and previously well-studied galaxies (Pickles 1985). The values of their R statistics (defined as the ratio of the correlation peak height to the amplitude of the antisymmetric noise) are listed in Table 2 along with the measured velocities and there formal uncertainties. For spectra with $R \prec 3.0$ the measured velocity was considered unreliable and was not used, except for emission-line

[1] IRAF is distributed by the National Optical Astronomy Observatories, which are operated by the Association of Universities for Research in Astronomy, Inc., under cooperative agreement with the National Science Foundation.

[2] The NED is operated by the Jet Propulsion Laboratory, California Institute of Technology, under contract with the National Aeronautics and Space Administration.

[3] This research has made use of data obtained from the superCOSMOS Science Archive, prepared and hosted by the Wide Field Astronomy Unit, Institute for Astronomy, University of Edinburgh, which is funded by the UK Science and Technology Facilities Council.

Table 2. Positions, photometric data and velocities for galaxies of AC114. The *R* column is the correlation peak height to the amplitude of the antisymmetric noise (see text for explanation).

Gal.	RA (J2000)	Dec. (J2000)	B_j (mag)	R_f (mag)	R_{comp} (mag)	Redshift	Error	*R*	Notes
Quadrant 1									
1	22 59 20.70	−34 42 24.6			20.0	0.39 852	0.00 030	3.50	em:H α,S1
2	22 59 31.37	−34 42 28.4			20.5	0.35 306	0.00 018		em:O II,H β,2O III,H α,S1
3	22 59 33.46	−34 42 39.8			18.0	0.05 717	0.00 011		em:H β,2O III,H α,S1
5	22 59 32.31	−34 42 58.2	20.2		20.1	0.05 842	0.00 009		em:H β,2O III,H α,S1
8	22 59 36.51	−34 43 25.4	20.2		20.3	0.38 058	0.00 022		em:H α,S1
9	22 59 25.99	−34 43 31.9				0.21 032?			Very uncertain
10	22 59 18.60	−34 43 43.6	20.5	18.8	18.9	0.21 940	0.00 024	4.76	em:H α,S1 65 840 km s^{-1}
11	22 59 17.61	−34 43 57.1			19.3	0.31 185	0.00 019	3.27	
12	22 59 20.05	−34 44 09.4	20.8	19.5	18.2	0.22 127	0.00 012	3.56	em:H β,H α 66 509 km s^{-1}
13	22 59 20.00	−34 44 20.3			20.0	0.40 980	0.00 028	4.48	
15	22 59 28.09	−34 44 29.0			19.4	0.07 309	0.00 045		em:H β,2O III,H α
16	22 59 28.82	−34 44 44.1			18.6	0.40 823	0.00 029	3.61	
17	22 59 38.42	−34 44 52.4			20.5	0.34 606	0.00 029	3.04	Very weak
18	22 59 23.15	−34 45 03.0			19.7	0.31 301	0.00 007		em:H α,S1
19	22 59 18.51	−34 45 13.1	21.2	20.3	19.6	0.40 876	0.00 022		em:O II,H β,2O III,H α,S1
20	22 59 40.37	−34 45 21.8			18.1	0.23 192	0.00 018	5.23	
22	22 59 24.80	−34 45 36.6	22.3	19.6	18.8	0.41 015	0.00 025	5.19	em:H β,H α
24	22 59 28.59	−34 45 49.8	21.6	19.6	18.9	0.33 369	0.00 018	4.84	em:O II
25	22 59 35.08	−34 45 57.0	22.4		20.9	0.32 344	0.00 028	3.12	
26	22 59 32.09	−34 46 13.6			19.6	0.40 926	0.00 027	3.65	
27	22 59 32.34	−34 46 23.3			19.9	0.46 615	0.00 022	3.22	
28	22 59 26.16	−34 46 32.5	20.2	19.2	19.0	0.35 118	0.00 028	3.11	Weak
30	22 59 36.18	−34 46 43.1	20.8	18.8	19.6	0.31 860	0.00 033	3.15	
31	22 59 33.65	−34 46 49.2			19.9	0.33 342			Measured on H α
34	22 59 25.25	−34 47 05.9			20.0	0.32 794	0.00 042	3.02	Very weak
36	22 59 34.22	−34 47 19.9			19.6	0.33 300	0.00 027	3.12	Very weak
37	22 59 23.76	−34 47 27.4	21.0	19.8	19.6	0.31 604	0.00 004		em:H β,2O III,H α,S1
38	22 59 18.07	−34 47 39.8			19.9	0.30 236	0.00 016	3.10	
40	22 59 23.41	−34 47 57.6	20.6	18.9	18.1	0.32 283	0.00 027	3.37	em:H β,2O III,H α,S1: 96 857 km s^{-1}
41	22 59 16.77	−34 48 06.8			20.0	0.32 061	0.00 045		
44	22 59 15.92	−34 48 43.8	22.2	21.1	19.1	0.28 628?	0.00 060	4.04	Uncertain
45a	22 59 31.40	−34 48 50.3				0.35 159			Measured on H α,S1
45b	22 59 31.40	−34 48 50.4				0.34 461			Measured on H α,S1
Quadrant 2									
1a	22 59 16.30	−34 33 40.6	20.8	19.0	19.6	0.25 782	0.00 023	3.43	em:H β,2O III,H α
1b	22 59 16.30	−34 33 40.6				0.33 069	0.00 024	3.18	em:H α, two galaxies
2	22 59 18.23	−34 33 50.7			18.2	0.49 578	0.00 029		em:O II,H β,2O III,H α,S1
3	22 59 18.00	−34 33 58.5			20.5	0.41 000	0.00 033		em:O II,H β,2O III,H α
4	22 59 13.67	−34 34 11.1			19.3	0.40 846	0.00 033		em:H β,2O III
5	22 59 15.03	−34 34 23.5	22.5	20.1	18.8	0.41 440	0.00 034	3.01	Very uncertain
6	22 59 23.91	−34 34 32.7	21.3	19.2	18.9	0.42 284	0.00 021	6.45	
7	22 59 21.45	−34 34 41.8			18.6	0.23 156	0.00 024	3.36	Very weak
8	22 59 12.89	−34 34 48.4			21.2	0.44 924	0.00 018	3.03	Weak
9	22 59 17.73	−34 34 54.1			20.9	0.31 359?			Very uncertain
10	22 59 18.77	−34 35 02.2	21.5	19.9	19.5	0.40 848	0.00 023	3.36	
11	22 59 16.88	−34 35 08.5			17.6	0.34 546			Measured on H α
12	22 59 32.84	−34 35 24.7	21.9		19.2	0.34 646	0.00 021	3.08	em:H α
13	22 59 26.31	−34 35 32.2			17.8	0.27 013	0.00 038	3.52	Very weak
14	22 59 20.21	−34 35 43.7			18.7	0.37 370	0.00 009		em:O II,H α,S1
15	22 59 15.61	−34 35 51.1			20.7	0.41 045	0.00 026	4.01	
16	22 59 19.18	−34 35 59.7	21.4	20.4	19.7	0.34 469	0.00 021	3.41	
18	22 59 12.16	−34 36 28.0	21.0		19.4	0.38 110	0.00 042	4.03	
19	22 59 19.31	−34 36 38.6	22.00	20.1	18.8	0.37 706	0.00 021	6.71	
21	22 59 21.69	−34 36 53.5			19.2	0.41 304	0.00 020	6.52	
22	22 59 36.79	−34 36 53.5			21.3	0.39 104			em:H α
23	22 59 21.57	−34 37 07.8	19.3	18.4	18.3	0.41 310	0.00 022	6.81	
24	22 59 36.81	−34 37 21.2			19.2	0.37 972	0.00 052		em:O II,H β,2O III
26	22 59 12.34	−34 37 37.5	22.3	20.2	19.4	0.48 676	0.00 018		em:O II,H β,2O III
27	22 59 21.00	−34 37 46.0	20.6	20.0	19.9	0.49 642	0.00 024	4.53	
28	22 59 15.56	−34 37 57.2	20.8	19.4	19.7	0.47 064	0.00 027	3.16	
29	22 59 17.62	−34 38 03.8			20.9	0.39 781	0.00 055	3.06	Very weak, uncertain

Table 2 – *continued*

Gal.	RA (J2000)	Dec. (J2000)	B_j (mag)	R_f (mag)	R_{comp} (mag)	Redshift	Error	R	Notes
31	22 59 24.67	−34 38 18.4	21.4	20.6	18.5	0.49 717	0.00 016		em:O II,H β,2O III,H α
32	22 59 25.00	−34 38 35.6	20.8	19.5	19.5	0.30 913	0.00 028		em:H β,2O III,H α
33	22 59 16.65	−34 38 43.7	20.1	18.1	20.4	0.46 922	0.00 051	3.17	em:H β 140 472 km s^{-1}
35	22 59 40.57	−34 39 05.1			19.7	0.31 290	0.00 016	7.72	
36	22 59 25.79	−34 39 11.8	21.4	20.0	19.8	0.46 367	0.00 020	6.71	
37	22 59 13.94	−34 39 33.0	21.8	20.7	18.7	0.32 064	0.00 016	3.42	
38	22 59 23.08	−34 39 47.1			20.1	0.29 869	0.00 017		em:H β,2O III,H α,S1
39	22 59 39.01	−34 39 53.1			20.6	0.37 203	0.00 012		em:O II,H β,2O III,H α
40	22 59 36.39	−34 39 58.4			20.3	0.41 913	0.00 023	4.96	
41	22 59 43.80	−34 40 06.7			20.5	0.31 907	0.00 026	3.08	
Quadrant 3									
1	22 58 41.57	−34 33 18.1	20.3	18.8	19.8	0.32 951	0.00 015		em:H β,2O III,H α,S1
2	22 58 41.21	−34 33 27.8	20.5	18.8	18.7	0.33 307	0.00 011		em:H β,2O III,H α,S1
3	22 58 40.11	−34 33 34.6	21.9	19.2	19.4	0.33 127	0.00 024	5.48	
4	22 58 40.08	−34 33 42.2	21.3	19.9	20.0	0.21 259	0.00 019		em:H β,2O III,H α,S1
5	22 58 41.10	−34 33 49.0			20.5	0.33 189	0.00 020		em:H β,2O III,H α,S1
6	22 58 33.87	−34 33 53.5			19.2	0.38 938?			Uncertain
8	22 58 42.73	−34 34 23.0	22.0		19.7	0.39 969	0.00 028	3.48	em:H α:119 724 km s^{-1}
10	22 58 22.64	−34 34 33.3	19.8	18.7	18.8	0.31 365	0.00 012	4.63	
11	22 58 35.95	−34 34 45.6	22.4	20.6	20.1	0.21 245	0.00 026		em:H β,2O III,H α,S1
12	22 58 36.88	−34 34 58.2	21.5	19.6	19.0	0.30 939	0.00 009		em:H β,2O III,H α,S1
13	22 58 51.29	−34 35 07.6			19.3	0.36 347	0.00 044	3.02	Very weak
15	22 58 41.00	−34 35 21.4			20.3	0.47 562	0.00 038	3.01	Very weak
16	22 58 45.84	−34 35 30.4	20.9	20.4	20.0	0.17 739	0.00 012		em:H β,2O III,H α,S1
17	22 58 48.43	−34 35 39.7			20.1	0.31 846	0.00 041	3.22	
18	22 58 56.50	−34 35 48.2	20.8	19.3	19.5	0.22 176	0.00 009		em:H β,2O III,H α,S1
19	22 58 23.26	−34 35 57.0	20.0	18.6	18.9	0.15 860	0.00 015	4.84	
20	22 58 32.46	−34 36 07.9			19.2	0.32 601	0.00 029	3.01	Very weak
21	22 58 32.39	−34 36 15.5	21.1	19.2	20.8	0.35 231	0.00 021		em:H β,H α,S1,S2
23	22 58 22.99	−34 36 26.7	22.1	20.5	20.5	0.43 221	0.00 036	3.39	
24	22 58 28.94	−34 36 34.7			18.2	0.30 386	0.00 045	3.01	Very weak
25	22 58 40.69	−34 36 41.1			20.1	0.47 190	0.00 039	3.15	
26	22 58 28.24	−34 36 48.7			20.2	0.31 477	0.00 024	4.07	
27	22 58 29.50	−34 36 55.9			19.6	0.41 028?			Uncertain
28	22 58 24.28	−34 37 02.1			18.4	0.25 761	0.00 018	5.51	
29	22 58 32.32	−34 37 07.5	21.6	20.1	20.6	0.47 283	0.00 038	3.15	
30	22 58 27.93	−34 37 16.9	21.2	20.1	21.1	0.40 221	0.00 023		em:O II, H β,2O III,H α
31	22 58 44.38	−34 37 24.2	22.2	20.2	20.1	0.39 764	0.00 040	3.04	em:H β,H α
33	22 58 39.09	−34 37 52.3			18.8	0.34 480			Measured on H α
34	22 58 39.66	−34 38 03.8			20.1	0.35 179	0.00 011		em:O II,H β,2O III,H α,S1
35	22 58 33.67	−34 38 18.9	21.4	20.1	18.9	0.43 091	0.00 014		em:H β,2O III,H α,S1
36	22 58 31.51	−34 38 24.2	22.3	20.7	20.5	0.20 326	0.00 031		em:H α,S1
38	22 58 41.21	−34 38 40.5			19.3	0.43 205	0.00 029	3.58	em: O II
39	22 58 46.63	−34 38 45.7	21.9	20.6	20.2	0.39 935	0.00 011		em:O II,H β,2O III,H α,S1
40	22 58 34.07	−34 38 53.1	21.9	19.9	19.3	0.31 828	0.00 031	4.12	
43	22 58 39.42	−34 39 13.5			20.2	0.27 849	0.00 033	3.11	
44	22 58 39.45	−34 39 24.1	22.2	19.4	19.5	0.22 464	0.00 017	3.34	em: H α,S1 67 344 km s^{-1}
45	22 58 43.50	−34 39 32.3	21.6	20.6	20.1	0.32 099	0.00 020	3.07	
46	22 58 42.70	−34 39 40.6			20.4	0.32 952	0.00 034	3.02	Very weak
49	22 58 37.09	−34 40 06.8	19.4	18.2	18.9	0.20 657	0.00 019	4.82	rm:H α,S1 61 753 km s^{-1}
Quadrant 4									
2	22 58 34.99	−34 42 24.0			19.5	0.31 982	0.00 035	5.82	em:H α weak
3	22 58 45.17	−34 42 28.9	22.6	19.1	20.1	0.32 038	0.00 021	3.18	
4	22 58 35.53	−34 42 35.8			19.7	0.31 108	0.00 014	3.42	
5	22 58 42.57	−34 42 42.5			20.6	0.42 558	0.00 012		em:H β,2O III,H α,S1
7	22 58 32.37	−34 42 55.1	20.4	19.7	20.0	0.16 952	0.00 009		em:H β,2O III,H α,S1
8	22 58 32.75	−34 43 02.0			19.5	0.17 061	0.00 022		em:H β,2O III,H α,S1
9a	22 58 31.70	−34 43 18.8	21.0	18.9	18.4	0.29 095	0.00 009	10.95	
9b	22 58 31.70	−34 43 18.8				0.25 733			em:H α
10	22 58 25.31	−34 43 25.5	20.5	18.8	19.5	0.31 228			em:H α very weak
11	22 58 32.43	−34 43 30.3	19.0	17.4	20.0	0.30 473	0.00 008	3.02	Very weak
12	22 58 26.84	−34 43 34.1	22.1	21.0	19.7	0.31 166	0.00 026	3.05	
13	22 58 26.64	−34 43 44.0	22.4	20.5	20.9	0.47 564	0.00 016	3.40	

Table 2 – *continued*

Gal.	RA (J2000)	Dec. (J2000)	B_j (mag)	R_f (mag)	$R_{\rm comp}$ (mag)	Redshift	Error	R	Notes
14	22 58 41.60	−34 43 46.5	20.5	18.9	20.7	0.30 460	0.00 007		em:O II,H β,2O III,H α,S1
15	22 58 25.91	−34 43 52.0	21.2	19.8	20.9	0.30 799	0.00 030		em:H β,2O III
16	22 58 29.50	−34 43 55.5	22.2	19.8	20.4	0.31 854	0.00 035	3.52	
18	22 58 25.81	−34 44 06.4			20.6	0.32 247	0.00 029	3.19	
19	22 58 26.24	−34 44 12.1			20.2	0.31 070	0.00 011		em:H β,2O III,H α,S1
20	22 58 39.44	−34 44 18.6			19.6	0.30 863	0.00 011		em:H β,2O III,H α,S1
21	22 58 50.72	−34 44 16.7			19.5	0.30 605	0.00 024	4.32	
22	22 58 39.87	−34 44 28.0			19.4	0.31 445	0.00 022	5.69	
23	22 58 35.11	−34 44 34.8	21.9		20.6	0.32 268	0.00 030	3.09	
24	22 58 33.19	−34 44 39.7			20.5	0.31 448	0.00 028	3.12	
25	22 58 30.22	−34 44 42.4			19.4	0.30 132	0.00 035	3.20	
26	22 58 42.00	−34 44 51.2	20.6	18.9	18.9	0.32 462	0.00 012		em:O II,H β,2O III,H α,S1
27	22 58 29.86	−34 44 55.5			21.4	0.31 265	0.00 023	3.08	
28	22 58 26.83	−34 45 02.6			20.0	0.31 467	0.00 032	3.53	
31	22 58 36.47	−34 45 17.4	21.0	19.3	19.1	0.31 779	0.00 024	5.33	
32	22 58 38.00	−34 45 24.1	20.2	17.7	18.2	0.31 708	0.00 024	5.65	
33	22 58 41.30	−34 45 30.6	21.1	19.6	19.8	0.10 193	0.00 029		em:O II,H β,2O III,H α,S1
35	22 58 47.92	−34 45 45.0	21.7	19.5	20.2	0.17 040	0.00 011		em:H β,2O III,H α,S1
36	22 58 35.91	−34 45 50.1	19.8	17.7	18.4	0.31 307	0.00 019	5.65	
37	22 58 29.65	−34 45 57.5			19.1	0.17 051	0.00 018	3.01	Uncertain
38	22 58 28.42	−34 46 02.3	22.0	19.8	19.2	0.30 100	0.00 026	5.63	
39	22 58 38.57	−34 46 10.7			20.1	0.32 594	0.00 047	3.43	
40	22 58 24.92	−34 46 18.7	20.8	19.0	19.0	0.31 779	0.00 004		em:H α
41	22 58 27.85	−34 46 26.3			19.7	0.31 816	0.00 033	4.55	
42	22 58 29.75	−34 46 32.1	22.2	20.5	19.9	0.50 228	0.00 035	3.04	
43	22 58 28.88	−34 46 40.3			20.2	0.31 717	0.00 033	3.68	
44	22 58 40.93	−34 46 45.7	20.6	18.6	18.3	0.31 523	0.00 030	4.73	
45	22 58 36.47	−34 46 51.2			20.6	0.31 389	0.00 019	4.66	
46	22 58 51.00	−34 47 00.6	20.8	19.5	20.1	0.32 953	0.00 028	3.10	
47	22 58 34.80	−34 47 07.1	22.2		19.3	0.31 674	0.00 019	6.24	
48	22 58 29.14	−34 47 13.1	21.6	20.0	20.0	0.31 462	0.00 022	5.29	
49	22 58 39.56	−34 47 17.4	21.8	19.1	20.0	0.31 818	0.00 024	4.89	
50	22 58 48.11	−34 47 21.3			20.2	0.33 032	0.00 039	3.02	Very weak
51	22 58 46.31	−34 47 31.5	20.8	18.8	19.1	0.30 954	0.00 019	6.32	
52	22 58 26.11	−34 47 37.5	22.6	20.9	18.2	0.38 782	0.00 037	3.04	Very weak
54	22 58 33.80	−34 47 46.6	22.3	19.5	18.9	0.34 779	0.00 030	3.06	Weak
55a	22 58 33.96	−34 47 53.3			20.2	0.31 776	0.00 031	3.26	
55b	22 58 33.96	−34 47 53.3				0.17 199			em:H β,2O III,H α,S1
56	22 58 44.05	−34 47 59.4			18.4	0.32 814	0.00 044	3.31	
57	22 58 49.74	−34 48 01.9	21.6	19.7	19.1	0.31 451	0.00 028	3.35	
58	22 58 41.65	−34 48 06.7	21.9	19.2	19.2	0.31 082	0.00 028	6.10	
59	22 58 45.48	−34 48 14.9			20.1	0.31 831	0.00 035	3.04	Weak
60	22 58 44.45	−34 48 21.3			19.0	0.32 473	0.00 031	4.42	
61	22 58 38.22	−34 48 27.8	20.7	18.6	19.7	0.72 072	0.00 014	3.05	
62	22 58 42.81	−34 48 33.4	21.0	18.9	29.9	0.31 090	0.00 047	5.43	
63	22 58 52.67	−34 48 39.1			20.2	0.31 874	0.00 024	4.98	
64	22 58 31.46	−34 48 53.3			18.3	0.31 447	0.00 030	5.28	
65	22 58 34.69	−34 49 01.3			20.6	0.47 788	0.00 023	5.33	

objects where the velocity was obtained using the EMSAO task implemented in the RVSAO package.

A total of 176 of the 200 observed spectra had S/N high enough to measure a useable velocity. Of these, 169 were galaxies, while 7 of them were found to be stars. Note that for four galaxies we derived two independent redshifts: object 45 in quadrant 1 with redshifts, respectively, 0.34461 and 0.35159, object 1 in quadrant 2 (0.25782 and 0.33069), and in quadrant 4 object 9 (0.25733 and 0.29095) and object 55 (0.17199 and 0.31776); after a visual inspection, these four targets seem to be composed of two objects in the line of sight. With our observations, we increase the number of galaxies with velocities in the field of AC114 by 32 per cent. Most of these are situated in the central region of the cluster. The new redshift values with their individual error measurements are published in Table 2 and correspond to the highest R-value obtained from the cross-correlations. We have constructed a velocity catalogue for AC114 with a total of 524 galaxies, where 169 are new measured velocities and 355 galaxies are from NED.

The contents of Table 2 are as follows:

(i) number of the object in each quadrant from slit position;
(ii) right ascension (J2000);
(iii) declination (J2000);
(iv) UK-J B_j magnitude from superCOSMOS (Maddox et al. 1990a,b);

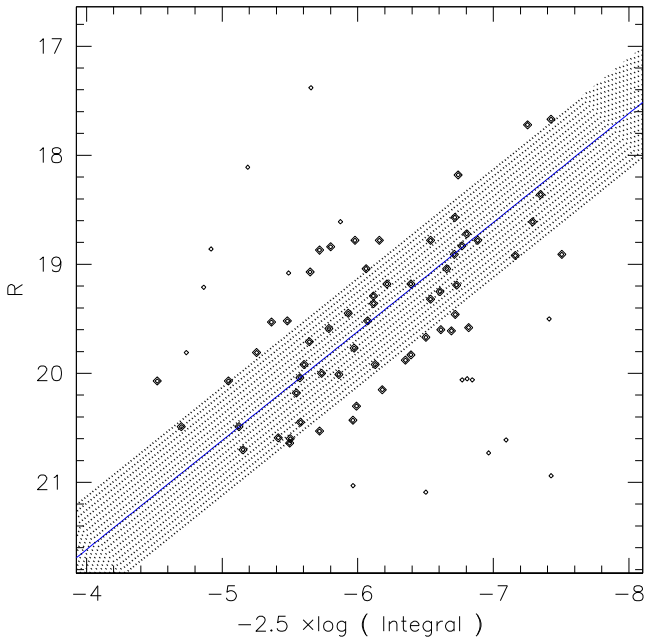

Figure 2. Relation between R_f magnitudes and the flux integral described in the text. Objects identified by larger symbols were considered in the linear regression, which is shown by the straight line. The shaded area represents the $\pm 1\sigma$ dispersion around the fit.

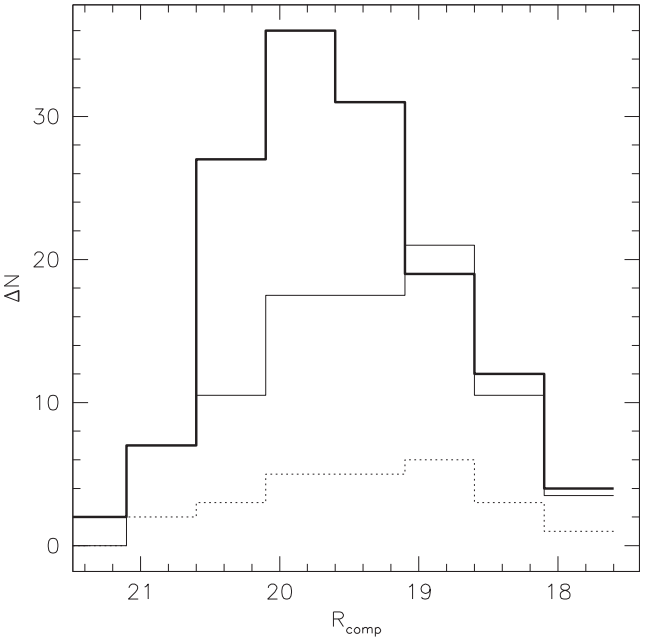

Figure 3. Luminosity distribution of galaxies with existing spectra (dotted-line histogram) and of galaxies added by the present study (thick-line histogram). To better compare the two samples, the thin-line histogram has been scaled from the dotted-line one so that the sum of counts in the three brightest bins is the same as that of the thick-line histogram. This scaling factor of 3.5 almost coincides with the ratio of the area surveyed by us and the area defined by literature data. *R*-band magnitudes were computed as described in the text.

(v) ESO-R or POSS-I E R_f magnitude from superCOSMOS (Maddox et al. 1990a,b);
(vi) $R_{\rm comp}$ computed magnitude from spectra;
(vii) redshift;
(viii) redshift error;
(ix) *R* value from the cross-correlation (Tonry & Davis 1979);
(x) notes.

Fig. 4 shows the wedge diagrams in RA and Dec. for both set of observed and NED galaxies out to 120 000 km s^{-1} with 468 galaxies; in the ∼10 arcmin × 10 arcmin central area of the cluster we have 189 velocities. Among the 169 velocities of table 2, 26 galaxies have previously published velocities listed in NED. Fig. 5 shows the velocity comparison for these 26 galaxies. It can be seen that NED velocities tend to be larger than those measured in this work, although this is just a 0.7σ effect. The dispersion is larger than our measurement errors, which is likely due to the non-homogeneity of the NED sample. We note a large velocity difference for the galaxy 56 in quadrant 4 of our table 2 (98 377 and 97 642 km s^{-1} from Couch et al. 1998). As our correlation coefficient is weak ($R = 3.31$) and our velocity error large (132 km s^{-1}) we give preference to their value.

Fig. 6 shows the sky distribution of emission-line galaxies (blue dots) and of passive galaxies (red dots) in our newly measured spectra for six different redshift ranges. There are 21 emission-line galaxies at the redshift of AC114 out of a total of 86 cluster members. The bottom panel shows that the fraction of emission-line galaxies has a dip at the redshift of AC114, and that these galaxies tend to avoid the cluster centre. Error bars in that panel show the 95 per cent confidence limits, calculated according to formula 3.27 in Feigelson & Babu (2013).[4] At such a redshift, all important emission lines still fall in the optical range, and the Universe is ≃70 per cent its current age, so we can expect a factor 1.4 increase in *Z* since that time, or 0.14 dex in $[m/H]$ (Gullieuszik et al. 2009, Leaman et al. 2013). A discussion concerning the MZR from this new set of emission-line galaxies is developed in Saviane et al. (2014) and Saviane et al. (in preparation).

3 VELOCITY ANALYSIS

Fig. 7 shows the redshift distribution of the spectroscopic sample within an area of ≃1.0 deg^2 centred on AC114. The large central peak at $z \sim 0.315$ corresponds to the main cluster. Other structures are seen, most for $z \leq 0.25$, as well also for $z \sim 0.41$. Note the important contamination by foreground and background objects along the line of sight: 45 per cent of the galaxies in our redshift catalogue are non-members of AC114. Couch & Sharples (1987) found it to be 18 per cent from 51 galaxies observed in a field of only 5 × 5 arcmin. In the same field we have 114 redshifts with a contamination rate of 23 per cent which is not significantly different.

We used the ROSTAT routines (Beers, Flynn & Gebhardt 1990) to analyse the galaxy velocity distribution of AC114. The dominant kinematical structure shown on Fig. 7 contains 265 galaxies between $z = 0.295$ and $z = 0.34$, including 77 new velocities. The rest-frame velocities $v = c(z - \overline{z})/(1 + \overline{z})$ range from −4312 to 3955 km s^{-1} at $\overline{z} = 0.31665^{+0.00072}_{-0.00082}$. The large rest-frame dispersion comes out as $\sigma = 1893^{+73}_{-82}$ km s^{-1} suggesting that the cluster could

[4] We have assumed that for our relatively large samples, the binomial distribution can be approximated by a normal distribution, so that $z_{\alpha/2} = 1.96$ in the formula. No confidence intervals were computed for the lowest and the highest redshift bin where the Gaussian approximation to the binomial distribution does not hold.

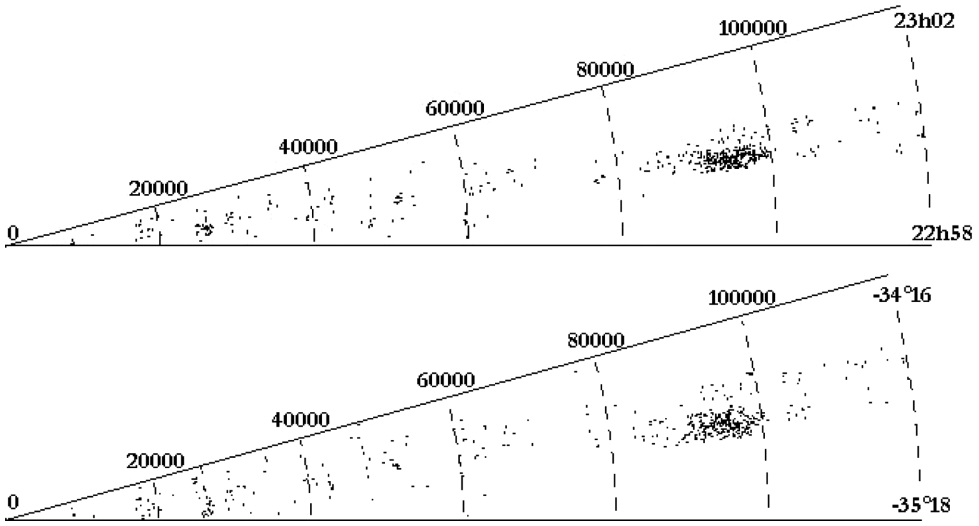

Figure 4. Wedge diagrams in RA and Dec. for both the newly observed and literature galaxies until 120 000 km s^{-1}.

be in a radial phase of relaxation with the presence of foreground and background structures. The very elongated radial filament spanning 12 000 km s^{-1} seen in Fig. 4 is a manifestation of the familiar *finger-of-god* effect due to this large internal dispersion velocity. Note that all the normality tests included in the ROSTAT package fail to reject the null hypothesis of a Gaussian distribution for this sample.

We can deduce that AC114 has an Abell radius defined by $R_{\rm Abell}$(arcmin) $\sim 1.72/\overline{z}$, which gives $R_{\rm Abell} = 5.431$ arcmin (1.44 h^{-1} Mpc) with an angular size distance of 909 h^{-1} Mpc and a scale of 264.54 Kpc arcmin^{-1} (and a luminosity distance of 1560 h^{-1} Mpc from the mean redshift corrected to the Reference Frame defined by the 3K cosmic microwave background). Note that Couch & Sharples (1987) found a dispersion $\sigma = 1649^{+217}_{-156}$ km s^{-1} from a set of 42 galaxies in a square region of 5 × 5 arcmin (1.32 × 1.32 h^{-1} Mpc) and Mahdavi & Geller (2001) with $\sigma = 1660^{+128}_{-106}$ km s^{-1} within a radius of 4.45 arcmin (1.18/h_{50} Mpc). Finn et al. (2004) give a dispersion of $\sigma = 1390$ km s^{-1} with $r_{200} = 1.87/h_{100}$ (9.54 arcmin) and Just et al. (2010) obtain similar values with $r_{200} = 3.98/h_{70}$ Mpc radius with 196 galaxies: $\overline{z} = 0.31500$ and $\sigma = 1889^{+81}_{-74}$ km s^{-1}. Fig. 8 shows the rest-frame velocity

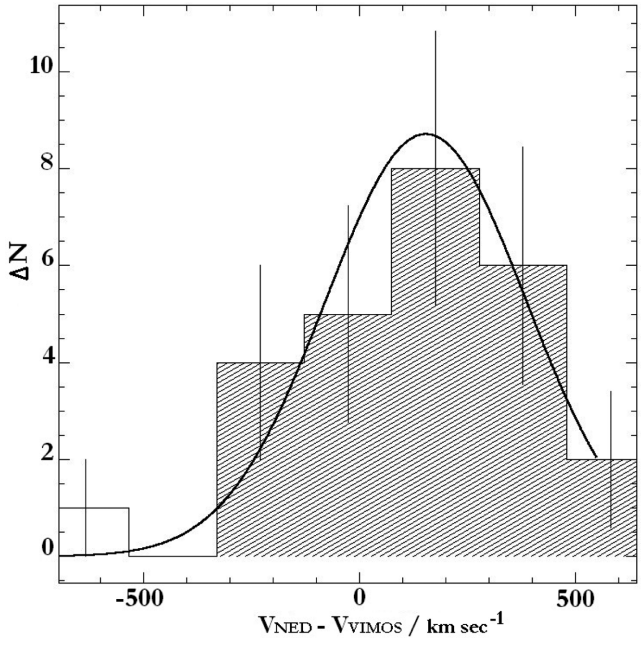

Figure 5. Velocity comparison between 26 velocities in common with this work (VIMOS) and the NED. After discarding the outlying galaxy with a very low NED velocity, the $v_{\rm NED} - v_{\rm VIMOS}$ distribution (shaded histogram) resembles a Gaussian one, albeit with a slight excess on the small values side. Velocity differences are distributed around the average 154 km s^{-1} with a dispersion of 232 km s^{-1}. The normal distribution with these parameters and the same area of the histogram is shown by the solid curve.

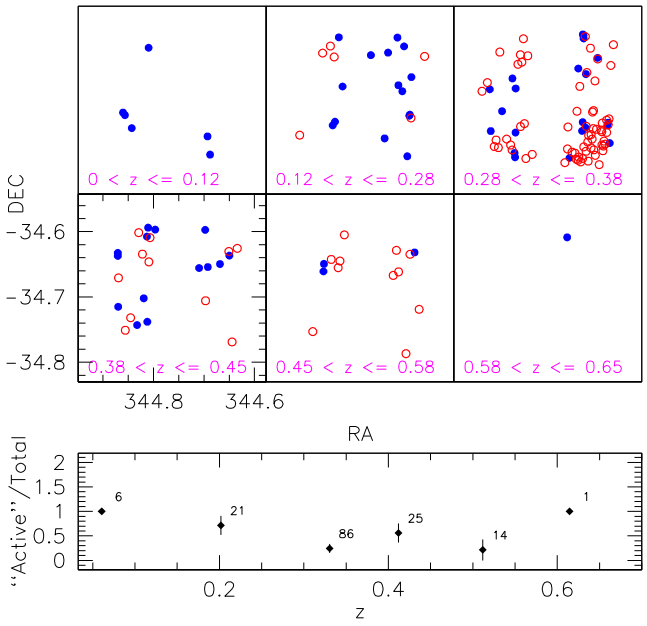

Figure 6. The top panels show the sky distribution of emission-line galaxies (blue dots) and of passive galaxies (red dots) for six redshift groups. The bottom plot shows the ratio of emission-line-to-total number of galaxies as a function of redshift. Error bars represent the 95 per cent confidence limits, and numbers near each point give the total number of galaxies for each redshift interval.

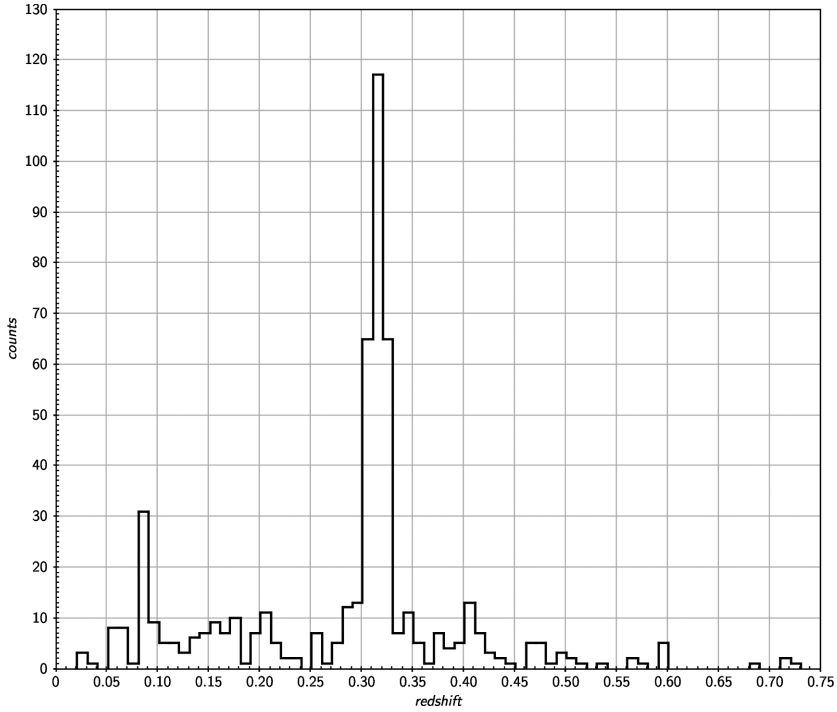

Figure 7. The redshift distribution within an area of $\sim$1.0 deg^2 centred on the AC114 cluster.

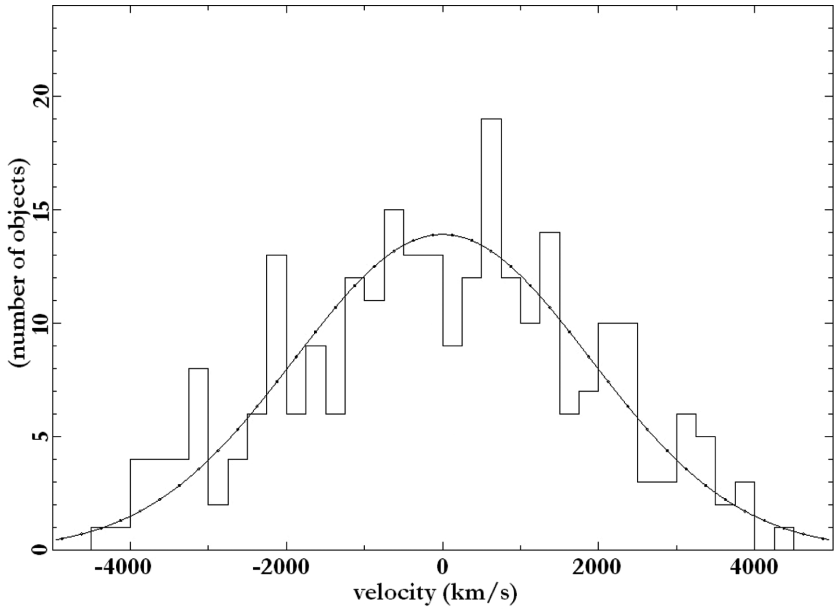

Figure 8. Rest-frame histogram of the velocity distribution of the AC114 cluster between 89 000 and 101 000 km s^{-1} with a step of 250 km s^{-1}; the Gaussian with $\sigma = 1893$ km s^{-1} (rest frame) is also shown.

histogram between 89 000 and 101 000 km s^{-1} and the Gaussian with $\sigma = 1893$ km s^{-1}.

The brightest cluster member (RA = 22$^{\rm h}$58$^{\rm m}$48$^{\rm s}$.4 Dec. = $-34^\circ 48' 08''$ J2000) has a redshift $z = 0.31\,691 \pm 0.00\,029$, very close to the average redshift of the cluster. This galaxy is not infrared-luminous compared with other massive early-type galaxies, suggesting that the cluster environment has little influence on the infrared luminosities of these galaxy as discussed by Martini, Mulchaey & Kelson (2007).

4 KINEMATICAL STRUCTURES

4.1 Method

In order to get more precise identifications of these structures, we applied the gap technique thoroughly discussed by Katgert et al. (1996). These consists in fixing a maximum allowed gap size in the rest-frame peculiar velocity space as a condition for galaxies to belong to a given structure. Adami et al. (1998) pointed out that gap sizes should not be kept constant, but should depend on the size

Table 3. Positions and redshifts of foreground, main and distant background structures of AC114.

Ident	RA	Dec.	z_{cl}	N_{gal} ($0.5\,h^{-1}$ Mpc)	$N_{gal}{}^a$ ($2.5\,h^{-1}$ Mpc)	Probability
AC114 main	22 58 45.6	−34 48 00	0.317 242	98	177	0.99
AC114 01	22 58 43.0	−34 46 34	0.301 921	4	17	0.77
AC114 02	22 59 06.2	−34 46 16	0.409 360	3	10^b	0.60

Notes. [a]After running the shifting gapper procedure to remove interlopers.
[b]Not confirmed by shifting gapper.

N_S of redshift sample since it is more likely to find large gaps in sparse data sets than in the richer ones, whereas a fixed gap would tend to overestimate the number of groups when N_S is small. Based on simulations of Gaussian distributions with varying number of objects they define the *density gap* such that

$$\Delta v_{max} = \delta_{gap} \times f(N_S) \quad (1)$$

with

$$f(N_S) = (1 + \exp(-(N_S - 6)/33) \quad (2)$$

and $\delta_{gap} = 500\,km\,s^{-1}$. In redshift space this translates to

$$\Delta z_{max} = (500/c)(1 + z_{cl}) f(N_S), \quad (3)$$

where z_{cl} is the mean redshift of the candidate structure and c is the speed of light in $km\,s^{-1}$.

We ran this gapping procedure for each of the candidate structures observed in the histogram displayed in Fig. 7. Following Lopes et al. (2009; see also Ribeiro et al. 2013) we start by first looking at their densest central region, assumed to be circular with 0.5 h^{-1} Mpc radius. We assume the central position of the main cluster as the initial guess for the calculations and further refine the central position of each candidate structure after collecting the galaxies belonging to the z-groups associated with it and re-starting the whole procedure. The z-groups detected by the gapping have their mean (bi-weighted) redshift $\bar{z}_\nu$ estimated and ranked accordingly to their distance to the nominal redshift of the candidate kinematical structure, $\delta_{\bar{z}} \equiv |\bar{z}_\nu - z_{cl}|$, with the most nearby being identified to it, providing

$$\delta_{\bar{z}} \leq \Delta v_{max}(1 + z_{cl})/c \quad (4)$$

with $\Delta v_{max} = 1000\,km\,s^{-1}$, allowing for the uncertainties and biases affecting the estimate of z_{cl}. Normally only one group survives this criteria and we then assume $z_{cl} = \bar{z}_\nu$ for this candidate structure. A new central sky position is calculated from the positions of the galaxies belonging to this z-group and the whole procedure is iterated once. Next we search for the extreme values z_{min}, z_{max} of the redshift distribution of the structure and then select all galaxies within 2.5 h^{-1} Mpc from its centre according to

$$|z_i - z_{cl}| \leq \max\{(z_{cl} - z_{min}), (z_{max} - z_{cl})\}. \quad (5)$$

We gauge the significance of the kinematical structures identified so far by bootstrap re-sampling the full redshift distribution found inside the 0.5 h^{-1} Mpc radius around its centre and re-applying the whole procedure exactly as before. We do that $N_{boot} = 1000$ times and then check the probability of detection of the group:

$$p(\bar{z}_\nu) = \frac{N_+(\bar{z}_\nu)}{N_{boot}}, \quad (6)$$

where $N_+(\bar{z}_\nu)$ is the number of positive detections for the group $\bar{z}_\nu$.

Finally, in order to reject possible interloper galaxies we apply the 'shifting gapper' technique (Fadda et al. 1996; Lopes et al. 2009), which consists on the same gapping procedure as described above but applied within radial bins of width $\geq 0.4\,h^{-1}$ Mpc containing at least 15 galaxies. The maximum redshift gap is now fixed at

$$\Delta z_{max} = (300/c)(1 + z_{cl}) f(N_S) \quad (7)$$

and we require that the mean redshift of the group does not deviate from z_{cl} by more than $\delta_{\bar{z}} \leq 300(1 + z_{cl})/c$. If no z-group is found satisfying these requirements the procedure stops and the aperture radius of the structure is identified to the internal radius of the bin.

4.2 Results

We limited our analyses to the interval $0.25 \leq z \leq 0.5$, which contain the main peak due to AC114 as well as neighbours foreground and background structures which may or may not interact with the main cluster. Table 3 displays the main parameters of the kinematical structures we have found. Besides the main cluster AC114, which dominates Fig. 7, we have been able to detect two others secondary structures although at low levels of significance. Fig. 9 (upper panel) shows the resulting redshift distribution of these structures and Fig. 9 (lower panel) shows with different symbols the projected positions of their galaxies.

The foreground structure AC114 01 seems to be much more relevant for our discussion on the evolutionary status of the main cluster. Although being detected as a redshift group of only four galaxies within the central 0.5 h^{-1} Mpc radius, and as so suggesting to be a mere statistical fluctuation of the phase space distribution of galaxies, we argue that, besides the 77 per cent of chances of detection (on 1000 bootstrap trials), this structure is still recognizable as a redshift group at the same central redshift value (within $c\delta_z \sim 300\,km\,s^{-1}$) at projected distances far from its very centre. In fact the shifting gapper was able to follow it out to $3.03/h_{73}$ Mpc which is ∼90 per cent of the limiting radius 2.5 h^{-1} Mpc. Given their proximity in redshift space – almost certainly reflecting their relative space configuration – it is very difficult to completely disentangle the redshift distribution of AC114 01 from that of the main cluster. Nevertheless we have been able to make roughly estimates of the population of interloper galaxies of AC114 01. In principle these should be constituted else by galaxies in their way of being torn from AC114 01 by the main cluster or by galaxies already dynamically linked to it.

Finally, as it can be seen from Fig. 9 (lower panel), the galaxies taking part of AC114 02 are sparsely distributed background to the main AC114 suggesting else they do not constitute a bound structure, or else the sky region it occupies has suffered of a bad sampling.

Note that if the relaxation occurs in two or more clusters in the line of sight, supporting evidence for this is extremely difficult to recognize with the existing data. Czoske et al. (2001, 2002) showed that the redshift distribution of the cluster Cl0024+17

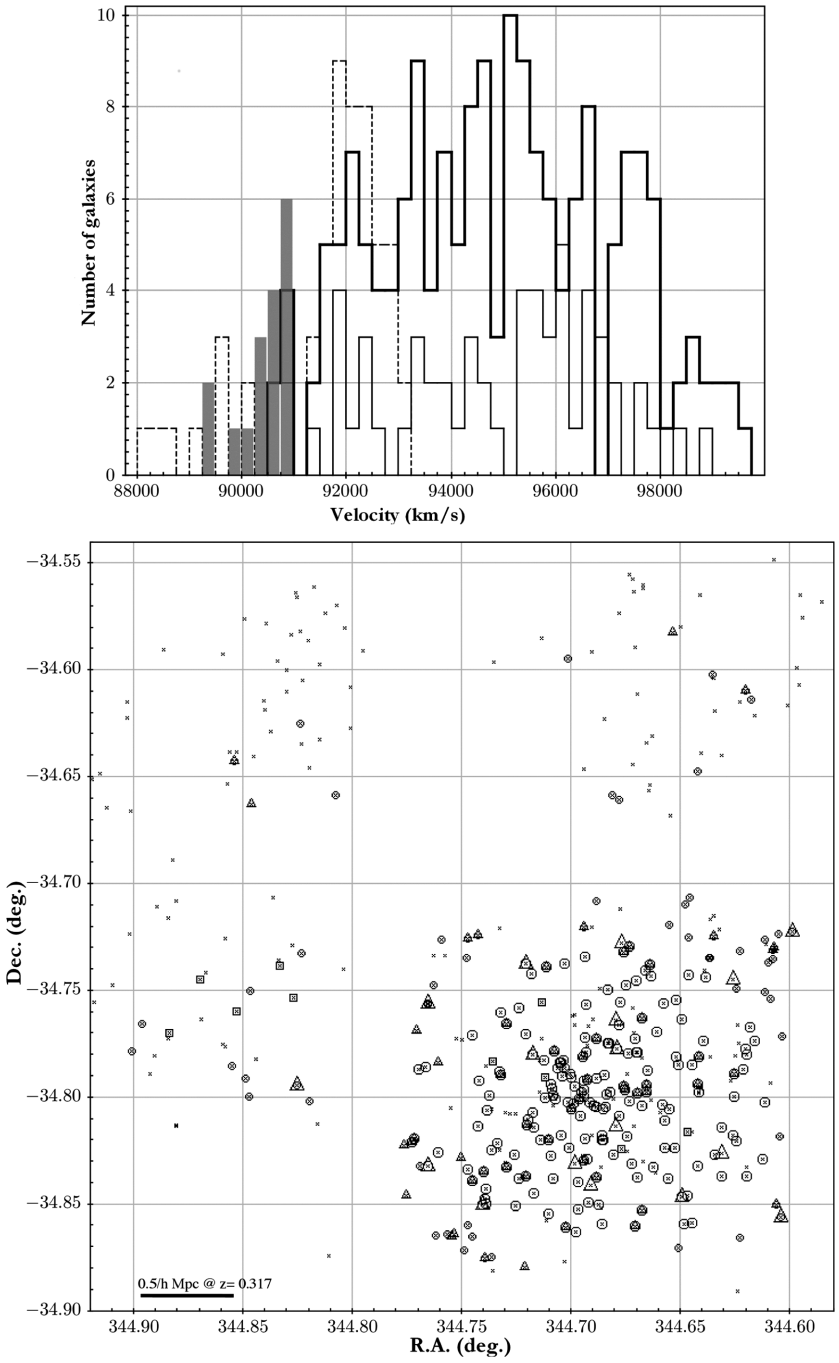

Figure 9. Upper panel: velocity histogram (step = 250 km s^{-1}) showing the main (heavy stepped line) and foreground (filled rectangles) structures detected as described in the text. The light stepped lines show the distribution of galaxies classified as interlopers for each of the structures. Lower panel: the projected distribution of galaxies of our spectroscopic sample (small crosses); large/small open circles show the positions of the galaxies belonging/interlopers to the main cluster, large/small open triangles give the positions of the foreground/interlopers structures galaxies and small/open squares are for those belonging to the background structure (cf. Table 3).

($z = 0.395$) is bimodal with a large primary component and a second foreground one, separated by $v = 3000$ km s^{-1}, suggesting that the system is undergoing a radial high velocity collision (note that both AC114 and Cl0024+17 show BO effect, see the next section). The Cl0024+17 bimodality is confirmed by Zuhone et al. (2009) using a high-resolution *N*-body/hydrodynamics simulation of such a collision. In the case of AC114, comparing Fig. 7 with figs 1 and 3 of Czoske et al. (2002) suggests the foreground structure mentioned above as a distinct grouping although the foreground one of Cl0024+17 is much more clearly delineated.

Following Rood et al. (1972), Kent & Gunn (1982) and more recently Czoske et al. (2002), we have constructed the AC114 pseudo-phase diagram by plotting the redshift for each galaxy versus its projected distance from the cluster centre on Fig. 10. The well-sampled part of AC114 corresponds to the very central part of the cluster Cl0024+17 extending 5 arcmin on the fig. 2 of Czoske

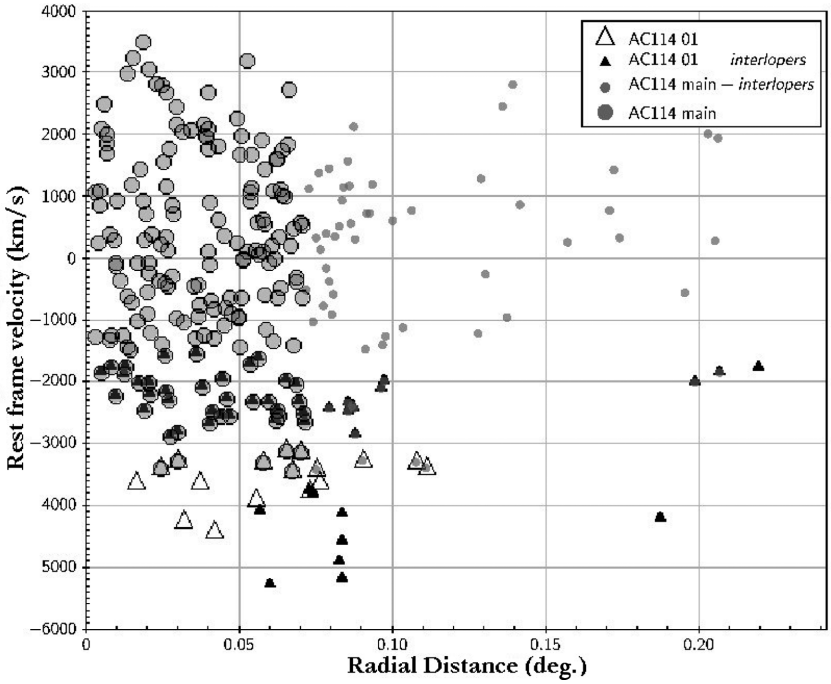

Figure 10. Relative velocity with respect to the mean cluster velocity plotted against angular distance R from the projected cluster centre for the galaxies around the cluster velocity. The left axis expresses relative velocity with respect to the mean velocity of the cluster; symbols are identical to Fig. 9.

et al. (2002). The distribution of the galaxies in the main peak is symmetrical with respect to the central redshift, whereas the distribution of the foreground galaxies is evidenced at a rest-frame velocity of $\simeq -5000\,\mathrm{km\,s^{-1}}$ at radii until 7 arcmin, but turns out towards smaller relative velocities to merge with the main distribution at smaller projected distances. The background galaxies velocity at a rest frame of $\simeq +4000\,\mathrm{km\,s^{-1}}$ are much more widely dispersed and we cannot rule out a connection with AC114; it seems more likely that they are part of the surrounding field galaxy population. Note the 'trumpet shaped' region extending horizontally from the cluster centre. The infall pattern around rich clusters of galaxies has been studied by Regos & Geller (1989) by constructing an analytic model for the distribution of galaxies around a cluster core in redshift space. From their fig. 6(b) showing the redshift as a function of the angular separation on the sky from the cluster centre, the high-density caustic surfaces which define the infall pattern show this characteristic trumpet shape. This shape is interpreted by these authors as the collapsing structure in which galaxies trace the matter distribution on the scale of the infall region and moreover, the caustics have a dependence on Ω_o. Such model has been tested by Regos & Geller (1989) for the rich clusters A539, Coma, A2670, A1367 and by Reisenegger et al. (2000) for the Shapley supercluster. Diaferio & Geller (1997) interpreted this trumpet shape as outlining the escape velocity profile rather than caustics due to the infall pattern. The appearance of Fig. 10 supports the reality of the foreground structure as it appears to lie mostly outside of the lower caustic. However, it is situated close to the limit of the virial radius of AC114. With a more complete set of velocities one could perhaps resolve definitively the dynamical status of AC114 and its immediate environs.

We also applied the method developed by Dressler & Shectman (1988) with the δ parameter to test for kinematical structures defined as

$$\delta^2 = (11/\sigma^2[(\overline{v}_{\mathrm{local}} - \overline{v})^2 + (\sigma_{\mathrm{local}} - \sigma)^2], \qquad (8)$$

where v_{local} and σ_{local} are the local velocities and dispersions calculated from the 10 nearest neighbours of each galaxy within the r_{200} radius which defines the limits of the virialized cluster from its redshift and velocity dispersion (i.e. with average density 200 times the critical one, see e.g. Diaferio et al. 2001; Finn et al. 2004):

$$r_{200} = 1.73 \frac{\sigma_{v,\mathrm{cl}}}{1000\,\mathrm{km\,s^{-1}}} \frac{1}{\sqrt{\Omega_\Lambda + \Omega_o(1+z_{\mathrm{cl}})^3}}\, h^{-1}\,\mathrm{Mpc}. \qquad (9)$$

In random redistributions of the measured galaxy velocities and positions, with $r_{200} \simeq 2.78\,h^{-1}$ Mpc we found the sum of the δ values to be equal to or larger than the observed value with a frequency of $P_\delta = 0.138$. This value is too marginal to conclusively verify the existence of substantial substructures. With $\sigma_{v,\mathrm{cl}} = 2025\,\mathrm{km\,s^{-1}}$ Martini et al. (2007) give $r_{200} \simeq 4.25/h_{70}$ Mpc and $P_\delta = 0.156$. Just et al. (2010) give $r_{200} = 3.98/h_{70}$ Mpc while Couch et al. (2001) use a value $r_v = 3.0/h_{100}$ Mpc.

5 GALAXY COLOUR DISTRIBUTION AND THE BO EFFECT

As UK-J B_j and ESO-R or POSS-I-E R_f magnitudes are available from superCOSMOS (Maddox et al. 1990a,b) a colour–magnitude diagram $B_j - R_f$ versus R_f for AC114 member galaxies identified from their redshift is shown in Fig. 11 (foreground and background objects have been removed). Note that plusses and crosses correspond, respectively, to absorption and emission-line galaxies observed by Couch & Sharples (1987), while squares and stars correspond to absorption and emission-line galaxies of this work and from various literature sources listed in NED, including the six AGN from Martini et al. (2006). The excess of blue galaxy cluster members ranging from 16 to 30 per cent is known as the BO effect (Butcher & Oemler 1978). As discussed by Couch & Sharples (1987), a 'red' galaxy sequence is defined with objects having $B_j - R_f \geq 2.0$. We identify this galaxy sequence extending to $R_f = 21.5$ distributed along the regression line on the top of the

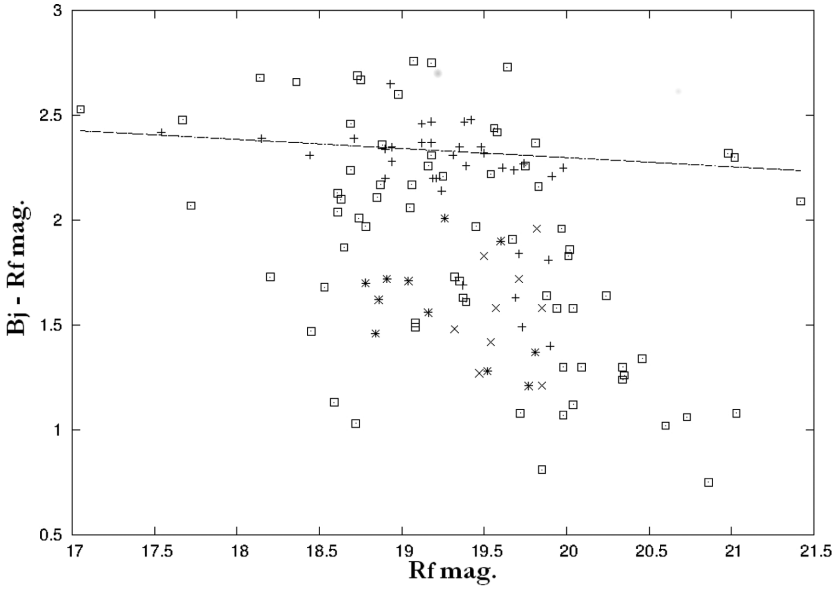

Figure 11. The $B_j - R_f$ diagram as a function of R_f for the AC114 cluster member galaxies within an Abell radius of 5.3 arcmin. (+) and (×) correspond, respectively, to absorption and emission-line galaxies observed by Couch & Sharples (1987), while squares and (*) are absorption and emission-line galaxies from our spectroscopic sample.

Fig. 11 with $B_j - R_f = -0.0435B_j + 3.169$. This sequence is well separated from the 'blue' galaxy area, where all emission-line galaxies are present. The ratio of emission/absorption-line galaxies belonging to AC114 is 19 per cent in Couch & Sharples (1987) and 24 per cent in this work. No obvious dynamical difference is seen between the red and blue populations as the red one with 47 objects gives $\overline{z} = 0.31\,757$ with $\sigma = 2019^{+115}_{-103}$ km s^{-1} and the blue one with 37 objects gives $\overline{z} = 0.31\,723$ with $\sigma = 1835^{+108}_{-121}$ km s^{-1}.

As quoted in Couch & Sharples (1987) BO cluster member galaxies represent 36 per cent of the total population in AC114, while Martini et al. (2007) found a ratio of 26 per cent brighter than $M_R = -20$ and we have 44 per cent of blue objects in this work. Such a discrepancy is a consequence of our galaxy sample, where most of them are located in the central region of AC114. It is also an effect of the larger number of galaxy cluster members with available photometry as well as the spectroscopy limiting magnitude of our sample which reaches magnitudes as faint as $R_f = 21.1$ (i.e. more than one magnitude fainter than the previous studies).

6 DYNAMICAL MASS DETERMINATIONS OF AC114

The mass of a cluster can be computed in several ways (Sereno et al. 2010). However, dynamical methods are based on the assumption that the cluster is close to equilibrium. In the case of AC114, as the foreground structure overlaps partially the main one, we considered the cluster as a whole. Assuming that galaxies are test particles orbiting in a dark matter spherical potential (Binney & Tremaine 1987), the expression for the virial mass of a cluster is

$$M_v = \frac{3\pi}{2}\frac{\sigma^2 R_{Pv}}{G} - C_{Pr}. \quad (10)$$

Here R_{Pv} is the projected virial radius of N observed galaxies and

$$R_{Pv} = \frac{N(N-1)}{\Sigma_{i>j} R_{ij}^{-1}}, \quad (11)$$

where R_{ij} is the projected distance between two galaxies given by i and j. C_{Pr} is a surface term which accounts that the system is not entirely enclosed in the observational sample with:

$$C_{Pr} = 4\pi r_{200}^3 \frac{\rho(r_{200})}{\int_0^{r_{200}} 4\pi r^2 \rho \mathrm{d}r}\left(\frac{\sigma_r(r_{200})}{\sigma(\prec r_{200})}\right)^2, \quad (12)$$

where $\sigma_r(r_{200})$ is the radial velocity dispersion at r_{200} and $\sigma(\prec r_{200})$ is the enclosed total velocity dispersion within r_{200} (Girardi et al. 1998). On average, for clusters observed within a radius of 1.5 h^{-1} Mpc, this correction is $\simeq$16 per cent (Biviano et al. 2006). The cluster AC114 has a redshift $z = 0.31\,665$ and a line-of-sight dispersion $\sigma = 1893$ km s^{-1} with $N = 265$ galaxies cluster members between 88 500 and 102 000 km s^{-1}. We obtain: $M_{200} = (4.3 \pm 0.7) \times 10^{15}$ M$_\odot$ h^{-1} enclosed within the virial radius. Our mass estimate is close to that derived by Sereno et al. (2010). For a mean redshift $z = 0.3153$ and a velocity dispersion $\sigma = 1900$ km s^{-1} they obtained $M_{200} = (3.4 \pm 0.8) \times 10^{15}$ M$_\odot$ h^{-1}.

The mass estimate can also be computed from the 3D intrinsic velocity dispersion σ_v within r_{200} (Biviano et al. 2006) with

$$M_v \equiv (1.5 \pm 0.02)\left(\frac{\sigma_v}{10^3 \text{ km s}^{-1}}\right)^3 \times 10^{14}\,\mathrm{M}_\odot\, h^{-1}. \quad (13)$$

The intrinsic velocity dispersion σ_v is corrected from the velocity dispersion profile following fig. 4 of Biviano et al. (2006) which gives for AC114 $M_v = (5.4 \pm 0.7 \pm 0.6) \times 10^{15}$ M$_\odot$ h^{-1}. Here, the first error is statistical, and the second one reflects the theoretical uncertainty on the relation (Sereno et al. 2010). Sereno et al. (2010) use this method to find a similar mass: $M_v = (4.8 \pm 0.8 \pm 0.6) \times 10^{15}$ M$_\odot$ h^{-1}. Note that Sereno et al. (2010) derived another mass estimate using the concentration parameter from a triaxial radius r_{200} such that the mean density contained within an ellipsoid of semimajor axis r_{200} is 200 times the critical density at the halo redshift. This method yielded a mass estimate $M_{200} = (1.3 \pm 0.9) \times 10^{15}$ M$_\odot$ h^{-1}.

Table 4. AC114 mass determinations as a function of the radius with different methods.

Radius (Mpc)	Mass (10^{14} $M_\odot$ h^{-1})	Error bar	Reference	Method
0.075	0.42	0.01	Natarajan et al. (1998)	Lensing
0.075	0.44	0.06	De Filippis et al. (2004)	X-ray
0.075	0.40	0.03	Sereno et al. (2010)	ICM, gal. haloes, DM
0.150	1.20	0.15	Natarajan et al. (1998)	Lensing
0.150	1.12	0.17	De Filippis et al. (2004)	X-ray
0.150	1.12	0.09	Sereno et al. (2010)	ICM, gal. haloes, DM
0.500	4.0	0.04	Natarajan et al. (1998)	Lensing
0.500	4.7	0.10	De Filippis et al. (2004)	X-ray
1.000	4.5	0.11	De Filippis et al. (2004)	$M_{\rm tot}$
3.98	34.0	8.0	Sereno et al. (2010)	Virial
3.98	43.0	7.0	This work	Virial
3.98	48.0	8.0	Sereno et al. (2010)	Biviano et al. (2006)
3.98	54.0	7.0	This work	Biviano et al. (2006)

De Filippis et al. (2004) derives X-ray masses from *Chandra* images with

$$M_{\rm tot}(1\,{\rm Mpc}) = (4.5 \pm 1.1) \times 10^{14} \times h_{72}^{-1}\,{\rm M}_\odot$$

$$M_{\rm gas}(1\,{\rm Mpc}) = (8.4 \pm 2.6) \times 10^{13} \times h_{72}^{-5/2}\,{\rm M}_\odot.$$

They compare their mass estimates with those obtained from weak and strong lensing by Natarajan et al. (1998) and conclude that they are in remarkably good agreement. Table 4 summarizes the available mass estimates from Natarajan et al. (1998), De Filippis et al. (2004), Sereno et al. (2010) and this work, in units of 10^{14} $M_\odot$ as a function of the radius in Mpc; the method used for mass determination is also indicated. We note that, despite the fact the mass determinations are made with a wide range of radial extents, they all appear to be fairly robust measurements with small relative errors, independent of the method used. If systematic biases exist, they have a weak influence on the results. As quoted in Biviano et al. (2006), projection effects have a significant impact on the reliability of cluster mass estimates through the inclusion of interlopers among the samples of presumed cluster members. In this work, we have only considered galaxies that are securely members of the main cluster and located inside the Abell radius. The presence of one foreground structure along the line of sight may lead to a higher level of uncertainty in the mass estimate presented.

7 SUMMARY AND CONCLUSIONS

(i) We have presented a dynamical analysis of the galaxy cluster AC114 based on a catalogue of 524 velocities of which 169 (32 per cent) are newly obtained at the ESO with the VLT and the VIMOS spectrograph.

(ii) We obtained an improved mean redshift value $z = 0.31\,665 \pm 0.0008$ and velocity dispersion $\sigma = 1893^{+73}_{-82}$ km s^{-1}. The cluster has a very elongated main radial filament spanning 12 000 km s^{-1} in redshift space.

(iii) Using Katgert et al. (1996) method, we have been able to detect two secondary structures although at low level of significance. A radial foreground one is detected within the central 0.5 h^{-1} Mpc radius, recognizable as a redshift group at the same central redshift value. The galaxies taking part of a background structure are sparsely distributed background to the main AC114, so that no conclusion can be given on a bound structure.

(iv) AC114 is an archetype BO galaxy cluster. We analysed the colour distribution for this galaxy cluster and identify the sequence of red galaxies which is well separated from the blue galaxies. The latter subset contains 44 per cent of confirmed members of the cluster, reaching magnitudes as faint as $R_f = 21.1$ (1.0 mag fainter than previous studies).

(v) From the spectroscopic data for $N = 265$ galaxies cluster members we derive a dynamical mass $M_{200} = (4.3 \pm 0.7) \times 10^{15}$ $M_\odot$ h^{-1} for AC114 and $M_v = (5.4 \pm 0.7 \pm 0.6) \times 10^{15}$ $M_\odot$ h^{-1} from the intrinsic velocity dispersion out to a radius of 3.98 h^{-1} Mpc.

The next phase of this study of AC114 will be to obtain direct metallicities of emission-line galaxies (Saviane et al. 2014). The redshift of AC114 puts it near the limit where VIMOS can be used to derive oxygen abundances via the T_e method, and this cluster is a well-known gravitational lens, with a number of photometric data sets already existing. At such a redshift, all important emission lines still fall in the optical range, and the Universe is $\simeq$70 per cent its current age, so we can expect a factor 1.4 increase in Z since that time, or 0.14 dex in $[m/H]$. A preliminary presentation of our metallicity analysis can be seen in Saviane et al. (2014).

ACKNOWLEDGEMENTS

We thank ESO-VLT staff for their assistance during the observations (program ID 083.A-0566A), and DP thanks ESO in the context of the *Visiting Scientists program* for its hospitality at Santiago (Chile). We also thank the referee for their very advised comments.

REFERENCES

Abell G. O., Corwin H. G., Olowin R. P., 1989, ApJS, 70, 1
Adami C., Mazure A., Biviano A., Katgert P., Rhee G., 1998, A&A, 331, 439
Allen S. W., 1998, MNRAS, 296, 392
Allen S. W., 2000, MNRAS, 315, 269
Beers T. C., Flynn K., Gebhardt K., 1990, AJ, 100, 32
Binney J., Tremaine S., 1987, Galactic Dynamics. Princeton Univ. Press, Princeton, NJ
Biviano A., Murante G., Borgani S., Diaferio A., Dolag K., Girardi M., 2006, A&A, 456, 23
Butcher H., Oemler A., 1978, ApJ, 219, 18
Campusano L. E., Pellò R., Kneib J. P., Le Borgne J. F., Fort B., Ellis R. S., Mellier Y., Smail Y., 2001, A&A, 378, 394
Colless M. et al., 2003, preprint (astro-ph/0306581)
Couch W. J., Sharples R. M., 1987, MNRAS, 229, 423
Couch W. J., Barger A. J., Smail I., Ellis R. S., Sharples R. M., 1998, ApJ, 497, 518

Couch W. J., Balogh M. I., Bower R. G., Smail I., Glazebrook K., Taylor M., 2001, ApJ, 549, 820
Cypriano E. S., Lima Neto G. B., Sodré L., Jr, Kneib J. P., Campusano L. E., 2005, ApJ, 630, 38
Czoske O., Kneib J. P., Soucail G., Bridges T. J., Mellier Y., Cuillandre J. C., 2001, A&A, 372, 391
Czoske O., Moore B., Kneib J. P., Soucail G., 2002, A&A, 386, 31
De Filippis E., Bautz M. W., Sereno M., Garmire G. P., 2004, ApJ, 611, 164
Diaferio A., Geller M. J., 1997, ApJ, 481, 633
Diaferio A., Kauffmann G., Balogh M. L., White S. D. M., Schade D., Ellingson E., 2001, MNRAS, 323, 999
Dressler A., Shectman S. A., 1988, AJ, 95, 284
Fadda D., Girardi M., Giuricin G., Mardirossian F., Mezzetti M., 1996, ApJ, 473, 670
Feigelson E. D., Babu G. J., 2013, Modern Statistical Methods for Astronomy. Cambridge Univ. Press, Cambridge
Finn R. A., Zaritski D., McCarthy D. W., Jr, 2004, ApJ, 604, 141
Girardi M., Giuricin G., Mardirossian F., Mezzetti M., Boschin W., 1998, ApJ, 505, 74
Gullieuszik M., Held E. V., Saviane I., Rizzi L., 2009, A&A, 500, 735
Hambly N. C., Irwin M. J., MacGillivray H. T., 2001, MNRAS, 326, 1295
Hamuy M., Walker A. R., Suntzeff N. B., Gigoux P., Heathcote S. R., Phillips M. M., 1992, PASP, 104, 553
Hamuy M., Suntzeff N. B., Heathcote S. R., Walker A. R., Gigoux P., Phillips M. M., 1994, PASP, 106, 566
Jones D. H. et al., 2009, MNRAS, 399, 683
Just D. W., Zaritsky D., Desai V., Rudnick G., 2010, ApJ, 711, 192
Katgert P. et al., 1996, A&A, 310, 8
Kent S. M., Gunn J. E., 1982, AJ, 87, 945
Kurtz M. J., Mink D. J., Wyatt W. F., Fabricant D. G., Torres G., Kriss G. A., Tonry J. L., 1991, in Worrall D. M., Biemesderfer C., Barnes J., eds, ASP Conf. Ser. Vol. 25, Astronomical Data Analysis Software and Systems I. Astron. Soc. Pac., San Francisco, p. 432
Larson R. B., 1974, MNRAS, 169, 229
Le Fèvre O., Crampton D., Lilly S. J., Hammer F., Tresse L., 1995, ApJ, 455, 60
Le Fèvre O. et al., 2003, in Iye M., Moorwood A. F. M., eds, Proc. SPIE Conf. Ser. Vol. 4841, Instrument Design and Performance for Optical/Infrared Ground-based Telescopes. SPIE, Bellingham, p. 1670
Leaman R. et al., 2013, ApJ, 767, 131
Leccardi A., Molendi S., 2008, A&A, 486, 359
Lopes P. A. A., de Carvalho R. R., Kohl-Moreira J. L., Jones C., 2009, MNRAS, 399, 2201
Maddox S. J., Sutherland W. J., Efstathiou G., Loveday J., 1990a, MNRAS, 243, 692
Maddox S. J., Efstathiou G., Sutherland W. J., 1990b, MNRAS, 246, 433
Mahdavi A., Geller M. J., 2001, ApJ, 554, L129
Martini P., Kelson D. D., Kim E., Mulchaey J. S., Athey A. A., 2006, ApJ, 644, 116
Martini P., Mulchaey J. S., Kelson D. D., 2007, AJ, 664, 761
Mellier Y., 1999, ARA&A, 37, 127
Mink D. J., Wyatt W. F., 1995, in Shaw R. A., Payne H. E., Hayes J. J. E., eds, ASP Conf. Ser. Vol. 77, Astronomical Data Analysis Software and Systems IV. Astron. Soc. Pac., San Francisco, p. 496
Natarajan P., Kneib J. P., Smail I., Ellis R. S., 1998, ApJ, 499, 600
Pickles A. J., 1985, ApJS, 59, 33
Pickles A. J., 1998, PASP, 110, 863
Regos E., Geller M. J., 1989, AJ, 98, 755
Reisenegger A., Quintana H., Carrasco E. R., Maze J., 2000, AJ, 120, 523
Ribeiro A. L. B., de Carvalho R. R., Trevisan M., Capelato H. V., La Barbera F., Lopes P. A. A., Schilling A. C., 2013, MNRAS, 434, 784
Rood H. J., Page T. L., Kintner E. C., King I. R., 1972, ApJ, 175, 627
Saviane I., Yegorova I., Proust D., Bresolin F., Ivanov V., Held E. V., Salzer J., Rich R. M., 2014, Mem. Soc. Astron. Ital., 85, 417
Sereno M., Lubini M., Jetzer Ph., 2010, A&A, 518, 55
Smail I., Couch W. J., Ellis R. S., Sharples R. S., 1995, ApJ, 440, 501
Tonry J., Davis M., 1979, AJ, 84, 1511
ZuHone J. A., Ricker P. M., Lamb D. Q., Karen Yang H. Y., 2009, ApJ, 699, 1004

This paper has been typeset from a TEX/LATEX file prepared by the author.